How to cite: *Angew. Chem. Int. Ed.* **2025**, *64*, e202418964
doi.org/10.1002/anie.202418964

VIP Heterogeneous Catalysis Very Important Paper

Single-Atom Pt Loaded on MOF-Derived Porous TiO_2 with Maximized Pt Atom Utilization for Selective Hydrogenation of Halonitrobenzene

Mingchun Guo[+], Qiangqiang Meng[+], Ming-Liang Gao, Lirong Zheng, Qunxiang Li, Long Jiao,* and Hai-Long Jiang**

Abstract: The location control of single atoms relative to supports is challenging for single-atom catalysts, leading to a large proportion of inaccessible single atoms buried under supports. Herein, a "sequential thermal transition" strategy is developed to afford single-atom Pt preferentially dispersed on the outer surface of TiO_2. Specifically, a Ti-MOF confining Pt nanoparticles is converted to Pt_{NPs} and TiO_2 composite coated by carbon (Pt_{NPs}&TiO_2@C-800) at 800 °C in N_2. Subsequent thermal-driven atomization of Pt_{NPs} at 600 °C in air produce single-atom Pt decorated TiO_2 (Pt_1/TiO_2-600). The resulting Pt_1/TiO_2-600 exhibits superior *p*-chloroaniline (*p*-CAN) selectivity (99 %) to Pt_{NPs}/TiO_2-400 (45 %) and much better activity than Pt_1@TiO_2-600 with randomly dispersed Pt_1 both outside and inside TiO_2 in the hydrogenation of *p*-chloronitrobenzene (*p*-CNB). Mechanism investigations reveal that Pt_1/TiO_2-600 achieves 100 % accessibility of Pt_1 and preferably adsorbs the $-NO_2$ group of *p*-CNB while weakly adsorbs –Cl group of *p*-CNB and *p*-CAN, promoting catalytic activity and selectivity.

[*] Dr. M. Guo,[+] Dr. Q. Meng,[+] Dr. M.-L. Gao, Prof. Dr. Q. Li, Prof. Dr. H.-L. Jiang
Hefei National Research Center for Physical Sciences at the Microscale, College of Chemistry and Materials Science, University of Science and Technology of China, Hefei, Anhui 230026 (P. R. China)
E-mail: liqun@ustc.edu.cn
jianglab@ustc.edu.cn
Homepage: http://mof.ustc.edu.cn/
Prof. Dr. L. Jiao
Key Laboratory of Precision and Intelligent Chemistry, University of Science and Technology of China, Hefei, Anhui 230026 (P. R. China)
E-mail: longjiao@ustc.edu.cn
Prof. Dr. L. Zheng
Beijing Synchrotron Radiation Facility, Institute of High Energy Physics, Chinese Academy of Sciences, Beijing 100049 (P. R. China)
[+] These authors contributed equally to this work.

Introduction

Single-atom catalysts (SACs) with metal oxides as supports have garnered significant attentions for a wide range of important reactions, such as hydrogenation reactions, CO oxidation, methane conversion and so on.[1] Ideally, SACs should simultaneously achieve the dispersibility and complete accessibility of active metal atoms to maximize their efficiency.[2] However, in practice, due to the uncontrollable location of single metal atoms, a large portion of single-atom sites are usually buried within the supports, becoming inaccessible and silent in catalysis, lowering their utilization efficiency far below the theoretical limit.[3] Since the catalytic process primarily occurs on the interface between catalysts and reactants, the preferential decoration of single-atom sites on the outer surface of the support holds great promise for maximizing their utilization and improving catalytic performance, while the controllable synthesis of targeted materials remains a great challenge.[4] To achieve this goal, two major challenges are waiting to be solved: (i) the construction of highly porous metal oxide supports with abundant and strong anchoring sites on their outer surface to stabilize single atoms, and (ii) the development of an effective way realizing the targeted landing of single metal atoms preferentially on the outer surface of supports.

Metal–organic frameworks (MOFs),[5] as a class of crystalline porous materials constructed by metal ions/clusters and organic linkers, have been extensively employed as ideal precursors/templates to produce porous carbons or metal oxides via high-temperature pyrolysis.[6] Some important features of pristine MOFs (high porosity, regular morphology, diverse components, etc.) can be largely inherited to their derived materials.[6a,b] While nitrogen-doped porous carbons derived from MOFs have been widely explored for supporting single metal atoms,[6c–f] the use of MOF-derived porous metal oxides as supports for single metal atoms has been relatively underexplored. MOF-derived metal oxide supports, with highly porous structure,[6i–j] provide abundant anchoring sites on their outer surface to trap isolated metal atoms and would be promising candidates to ensure the accessibility and stabilization of single atoms.

In addition to using porous supports with large surface area for single atom decoration, the decoration route of single metal atoms, which will determine their relative location on the support directly, is also of great significance

to dominate the accessibility and activity of single-atom sites.[7] The post-atom trapping route, such as the capture of single-metal atoms in vapor or liquid phase using a pre-formed oxide with strong lattice energy, can set larger barrier for the incorporation of external single atoms into the bulk phase, which is promising to ensure the dispersion of single metal atoms on the outer surface of supports.[8] The MOF-derived porous metal oxides (ideal supports with large surface areas to trap and stabilize single metal atoms), when combined with post-atom trapping (dominating the preferential location of single metal atoms on the outer surface of supports), would provide a rational way to design oxide supported single metal atoms with highly exposed sites.

In this work, a typical Ti-based MOF, named MIL-125, is employed as a host to confine Pt nanoparticles (Pt_{NPs}), affording Pt_{NPs}@MIL-125 composite as a precursor. Through a simple "sequential thermal transition" process, the Pt_{NPs}@MIL-125 is initially converted to Pt_{NPs} and TiO_2 composites confined in carbon layer (Pt_{NPs}&TiO_2@C-800) at 800 °C in N_2. Upon subsequent pyrolysis at 600 °C in air, the carbon layer is burnt off and Pt_{NPs} on TiO_2 undergo thermal atomization to form single-atom Pt species which are trapped on as-formed TiO_2, affording Pt_1/TiO_2-600 material (Scheme 1). By decoupling the themolysis of MOF to TiO_2 and Pt_1 capture on the MOF-derived TiO_2, the preferential dispersion of Pt_1 outside TiO_2 with 100 % Pt accessibility is successfully achieved. The resulting Pt_1/TiO_2-600 exhibits excellent activity and selectivity in the hydrogenation of *p*-chloronitrobenzene (*p*-CNB) to *p*-chloroaniline (*p*-CAN), surpassing Pt_{NPs}/TiO_2-400 (Pt_{NPs} on TiO_2) and Pt_1@TiO_2-600 (Pt_1 decorated outside and within bulk phase of TiO_2 simultaneously). Theoretical calculations reveal that the Pt_1 site in Pt_1/TiO_2-600 shows excellent adsorption and activation ability for the $-NO_2$ in *p*-CNB while inhibit the adsorption of –Cl, promoting the selective hydrogenation of *p*-CNB to *p*-CAN with high efficiency.

Results and Discussion

The Pt_{NPs}@MIL-125 composites were fabricated by in situ encapsulation of as-synthesized Pt_{NPs} (~3 nm) during the synthesis of MIL-125.[9] Powder X-ray diffraction (XRD) pattern of Pt_{NPs}@MIL-125 demonstrates the well-maintained MOF crystallinity (Figure S1). Scanning electron microscopy (SEM) image indicates the cake-like morphology of Pt_{NPs}@MIL-125 similar to the pristine MOF (Figure S2). Transmission electron microscopy (TEM) observation for Pt_{NPs}@MIL-125 displays the uniform dispersion of Pt_{NPs} inside MIL-125 (Figure 1a). When pyrolyzed at 800 °C in N_2, Pt_{NPs}@MIL-125 is converted to the Pt_{NPs} and TiO_2 composite coated by carbon layer (Pt_{NPs}&TiO_2@C-800) (Figure S3–S5). Subsequently, the obtained Pt_{NPs}&TiO_2@C-800 is further thermally treated in air under various temperatures (400 °C, 600 °C or 800 °C). For the sample treated in air at 400 °C, the carbon layer can be totally burnt off and obvious Pt_{NPs} can be identified, forming Pt_{NPs}/TiO_2-400 composite (Figure 1b and S6). When the heat treatment temperature is elevated to 600 °C in air, the TiO_2 support still presents well retained cake-like shape while no apparent Pt_{NPs} can be observed, implying the thermal atomization of Pt_{NPs} (Scheme 1, Figure S7). Aberration-corrected high-angle annular dark-field scanning transmission electron microscopy (HAADF-STEM) observation presents the isolated bright dots (labelled by red circles) on TiO_2, and clearly suggests the atomic dispersion of Pt in Pt_1/TiO_2-600 (Figure 1c). Moreover, N_2 sorption isotherm clearly indicates the highly porous structure of Pt_1/TiO_2-600 with a moderate surface area (44 m^2/g) which is beneficial to the stabilization of single-atom Pt (Figure S8). Unexpectedly, when the temperature of pyrolysis in air reaches 800 °C, single-atom Pt_1 sites (labelled by red circles) and Pt clusters (Pt_{clus}) (labelled by white circles) are both identified in Pt_{1+clus}/TiO_2-800, suggesting the partial sintering of Pt_1 at the temperature higher than 600 °C (Figure 1d). In addition, the actual mass contents of Pt in Pt_{NPs}/TiO_2-400, Pt_1/TiO_2-600 and Pt_{1+clus}/TiO_2-800 are determined to be well controlled in the narrow range of 0.39–0.49 wt % (Table S1).

X-ray photoelectron spectroscopy (XPS) analysis has been further performed to confirm the chemical state of Pt

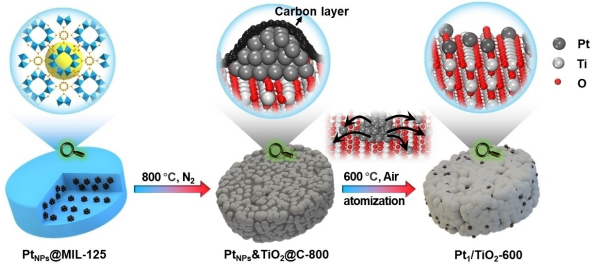

Scheme 1. Illustration for the construction of Pt_1/TiO_2-600 via a "sequential thermal transition" process.

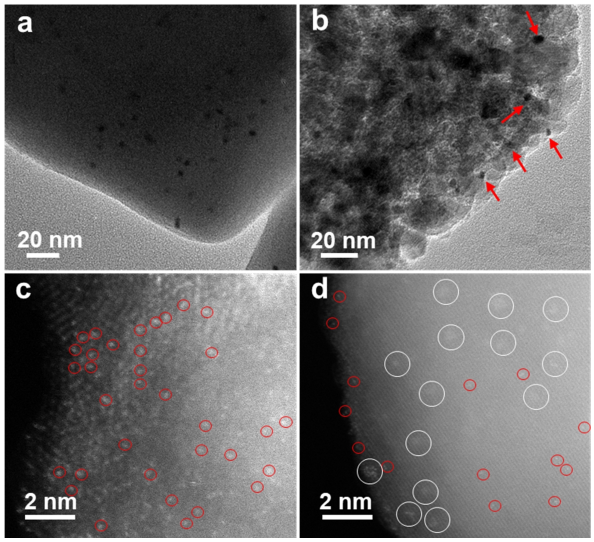

Figure 1. TEM images of (a) Pt_{NPs}@MIL-125 and (b) Pt_{NPs}/TiO_2-400. HAADF-STEM images of (c) Pt_1/TiO_2-600 and (d) Pt_{1+clus}/TiO_2-800 (The red circles highlight the single Pt atoms while the white circles indicate the presence of Pt clusters).

in the obtained samples. In the Pt 4f spectrum of Pt_1/TiO_2-600, only two peaks with binding energies at 74.5 and 77.8 eV, which are assigned to Pt^{4+}, are observed, revealing the atomic dispersion of Pt (Figure S9). In contrast, metallic Pt^0 species are both identified in Pt_{NPs}/TiO_2-400 and Pt_{1+clus}/TiO_2-800,[10] in accordance with the observed Pt clusters in TEM images (Figure S9 and 1d). Moreover, the Ti 2p spectrum presents peaks corresponding to the Ti $2p_{3/2}$ and Ti $2p_{1/2}$ of both Ti^{3+} and Ti^{4+} in Pt_1/TiO_2-600, while typical Ti^{4+} signals is only observed for Pt_{NPs}/TiO_2-400 (Figure S10). Moreover, the electron paramagnetic resonance (EPR) spectrum of Pt_1/TiO_2-600 further confirm the existence of Ti^{3+} (Figure S11). It has been reported Ti^{3+} can benefit the stabilization of Pt_1 by forming Pt–(O)–Ti bonds,[11] which might be responsible for the atomic dispersion of Pt in Pt_1/TiO_2-600.

To further study the electronic structures and coordination environment of Pt, X-ray absorption fine structure (XAFS) analysis has been performed. The X-ray absorption near edge spectroscopy (XANES) spectrum of Pt for Pt_1/TiO_2-600 shows a white-line peak much higher than metallic Pt yet close to PtO_2 (Figure S12), implying the positive valence state of Pt close to +4. In contrast, Pt_{1+clus}/TiO_2-800 show a lower white line peak intensity than PtO_2 and Pt_1/TiO_2-600 (Figure S12), suggesting the possibly lower oxidation state of Pt due to the formation of Pt clusters. Fourier transform-extended X-ray absorption fine structure (FT-EXAFS) spectrum of Pt_1/TiO_2-600 shows a dominant Pt–O coordination peak at 1.60 Å and a second shell peak at 3.2 Å, respectively attributing to Pt–O and Pt–(O)–Ti coordination, while no Pt–Pt coordination (~2.60 Å) is observed (Figure 2a), supporting the atomic dispersion of Pt in Pt_1/TiO_2-600.

Moreover, the wavelet transformed (WT) contour plot of Pt_1/TiO_2-600 presents a single intensity maximum at around ~7.0 $Å^{-1}$ in k space and ~1.6 Å in R space similar to the Pt–O contribution in the first shell of PtO_2, further confirming the atomic dispersion of Pt (Figure 2b). By curve fitting for EXAFS spectrum, the coordination number (CN) for Pt–O and Pt–(O)–Ti in Pt_1/TiO_2-600 are determined to be 5.7 and 4.1, respectively (Figure 2c, Table S2). The coordination environment of Pt in this case aligns best with the single-atom Pt dispersed on TiO_2 by occupying the position of Ti on the outer surface, which greatly benefits the exposure of Pt (Figure S13). Moreover, both EXAFS spectrum and WT contour plot of Pt_{1+clus}/TiO_2-800 suggest the Pt–O and Pt–Pt scatterings with CN values of 3.9 and 2.7, respectively, further indicating the coexistence of Pt_1 and Pt_{NPs} (Figure 2a, S14 and S15; Table S2).

To further evaluate the dispersion status of Pt in different samples, the diffuse reflectance infrared Fourier transform spectroscopy (DRIFTS) measurements of CO adsorption have been carried out. In the DRIFTS spectrum of Pt_1/TiO_2-600, only one sharp peak at 2096 cm^{-1} assigned to linear CO adsorption on single Pt atoms appears,[12] further confirming the exclusive existence of single-atom Pt sites (Figure 2d). By contrast, Pt_{NPs}/TiO_2-400 shows obvious signals of linear and bridge-bonded CO on Pt_{NPs} (Figure S16).[13] The Pt_{1+clus}/TiO_2-800 exhibits three distinct peaks centered at 2096, 2060 and 1820 cm^{-1} similar to Pt_{NPs}/TiO_2-400 (Figure 2d). The peaks centered at 2060 and 1820 cm^{-1} correspond to the linear and bridge adsorption modes of CO on metallic Pt respectively, manifesting the existence of Pt clusters in Pt_{1+clus}/TiO_2-800. The DRIFTS results together with HAADF-STEM and XAFS analyses give solid evidences for the thermal transformation from Pt_{NPs} to atomically dispersed Pt_1 in Pt_1/TiO_2-600. When the temperature is much higher (800 °C), re-agglomeration of Pt_1 sites takes place in $Pt_{1+clus}TiO_2$-800.

To confirm the effectiveness of "sequential thermal transition" strategy on dominating the preferential location of Pt_1, the CO pluse chemisorption experiments have been performed to determine the proportion of Pt_1 on the outer surface of TiO_2. It shows that about 5 pulses of CO are required to saturate the Pt_1 sites in Pt_1/TiO_2-600 (Figure 3a). The further precise calculations based on the CO pulse chemisorption experiments reveal that the proportion of Pt_1 sites which can adsorb CO reaches almost ~100 % in Pt_1/TiO_2-600, which means the complete exposure of Pt_1 sites on the TiO_2 surface (Figure 3b). For better comparison, $Pt_1@TiO_2$-600, with Pt_1 randomly dispersed on the outer

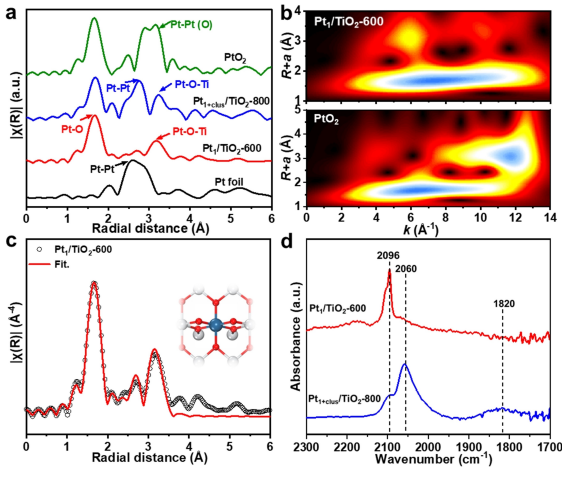

Figure 2. (a) The FT-EXAFS spectra of Pt_1/TiO_2-600 and Pt_{1+clus}/TiO_2-800. (b) WT contour plots of Pt_1/TiO_2-600 and PtO_2. (c) The EXAFS fitting of Pt_1/TiO_2-600 (inset: optimized coordination environment of single Pt atom). (d) DRIFTS spectra of CO adsorption on Pt_1/TiO_2-600 and Pt_{1+clus}/TiO_2-800.

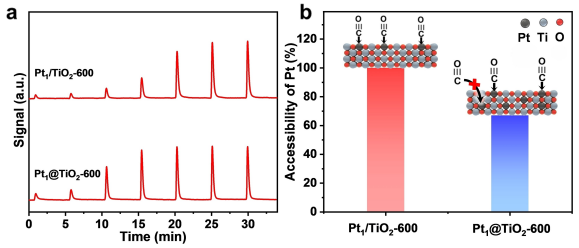

Figure 3. (a) CO pulse chemisorption at 308 K and (b) Accessibility of Pt_1 sites determined by CO pulse chemisorption of Pt_1/TiO_2-600 and $Pt_1@TiO_2$-600.

surface (accessible Pt_1) and incorporated in the bulk phase (inaccessible Pt_1) of TiO_2, is also fabricated through the one-step pyrolysis of MIL-125 containing $[PtCl_6]^{2-}$ (named $[PtCl_6]^{2-}$@MIL-125) instead of Pt_{NPs} (Scheme S1). In contrast to the decouple process of TiO_2 pre-formation and Pt_1 post-decoration for the preparation of Pt_1/TiO_2-600, the formation of crystalline TiO_2 is accompanied by single-atom Pt incorporation during $Pt_1@TiO_2$-600 fabrication, making it easy for the Pt atoms in $[PtCl_6]^{2-}$@MIL-125 to be confined into the resulting TiO_2. By EXAFS analysis, the atomic dispersion of Pt in $Pt_1@TiO_2$-600 is confirmed and the loading amounts of Pt in Pt_1/TiO_2-600 and $Pt_1@TiO_2$-600 are controlled at the same level (Figure S17, Table S1). However, the CO pulse adsorption of $Pt_1@TiO_2$-600 shows ~3 pulses of CO for saturated adsorption and smaller proportion (67 %) of Pt dispersed on the outer surface of TiO_2 than Pt_1/TiO_2-600 (Figure 3a). This clearly indicates the superiority of "sequential thermal transition" strategy to boost the full exposure of Pt_1 sites.

Based on the aforementioned results, the formation mechanism of Pt_1/TiO_2-600 can be illustrated as follows. As pyrolysis temperature of Pt_{NPs}&TiO_2@C-800 obtained from Pt_{NPs}@MIL-125 is set at 400 °C in air, the carbon layer is easily burnt off while the existence of Pt_{NPs} is undisturbed, forming a composite of Pt_{NPs} and TiO_2 (Pt_{NPs}/TiO_2-400). When the temperature elevates to 600 °C, the Pt_{NPs} start releasing mobile Pt–O gaseous species with the assistance of O_2 in air.[14] These Pt–O species would be trapped on the porous TiO_2, giving rise to the formation of Pt_1/TiO_2-600. Since the TiO_2 is pre-formed prior to the atomization of Pt_{NPs}, Pt atoms from Pt–O species are more energetically favorable to be trapped on the outer surface than incorporated into the bulk phase of TiO_2 (Figure S18). As a result, the preferential dispersion of Pt_1 on the outer surface of TiO_2 is achieved successfully, leading to a significant enhancement in the accessibility of catalytic sites.

Inspired by the results above, the catalytic performance of different samples has been evaluated in the selective hydrogenation of *p*-chloronitrobenzene (*p*-CNB) to obtain haloanilines (HANs), which are important organic intermediates widely used in medicine, pesticides, fuels, and chemicals.[15] Encouragingly, Pt_1/TiO_2-600 displays preeminent conversion (100 %) of *p*-CNB with an almost absolute selectivity (> 99 %) to *p*-chloroaniline (*p*-CAN), and the dechlorination process is significantly suppressed (Figure 4a). Moreover, the catalytic activity and selectivity to *p*-CAN of Pt_1/TiO_2-600 are much better than that of Pt_{NPs}/TiO_2-400 and Pt_{1+clus}/TiO_2-800, highlighting the superiority of Pt_1/TiO_2-600 (Figure 4a). As a reference, pure porous TiO_2-600 with Ti^{3+}, but without Pt, is also prepared from MIL-125 and shows negligible catalytic activity, further confirming the significance of Pt for the reaction (Figure S19a, S20 and S21; Table S3). Additionally, $Pt_1@TiO_2$-600, with Pt_1 randomly dispersed both outside and within TiO_2 (Figure S19b, Figure S20), is also employed for catalysis. Despite possessing very similar Pt_1 loading to Pt_1/TiO_2-600, $Pt_1@TiO_2$-600 displays much lower reaction rate than Pt_1/TiO_2-600 (Figure 4a, Table S1). This accounts for that Pt_1/TiO_2-600, with Pt_1 sites on the outer surface of TiO_2,

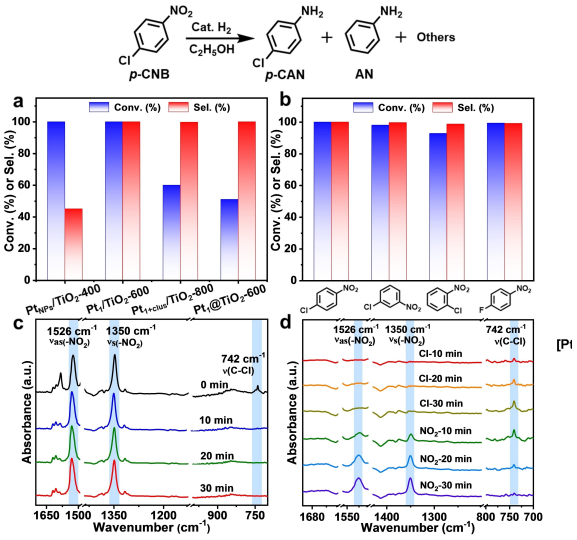

Figure 4. (a) Catalytic performance of different catalysts in the hydrogenation of *p*-CNB at 80 °C under 15 bar H_2 within 1.5 h. (b) The hydrogenation of various halogenated nitrobenzenes over Pt_1/TiO_2-600. (c) DRIFTS spectra for the competitive adsorption of nitrobenzene and chlorobenzene and (d) Adsorbate-displacement tests between nitrobenzene and chlorobenzene over Pt_1/TiO_2-600.

provides more accessible Pt_1 sites to reactants than $Pt_1@TiO_2$-600. Furthermore, even prolonging the reaction time to 3 h, Pt_1/TiO_2-600 still shows extraordinarily high selectivity (above 99 %) toward *p*-CAN (Figure S22a), which further underscores the excellent capability of Pt_1/TiO_2-600 for selective hydrogenation of $–NO_2$ while inhibiting dechlorination. Moreover, the excellent catalytic performance of Pt_1/TiO_2-600 to *p*-CAN can be well maintained in the three consecutive runs (Figure S22b). Meanwhile, both powder XRD pattern and TEM image of Pt_1/TiO_2-600 after catalysis confirm the absence of Pt agglomeration (Figure S23), highlighting the excellent stability of single Pt atoms.

In addition, the selective hydrogenation of diverse nitroarenes substrates have been also examined. It is found that 2-nitrochlorobenzene and 3-nitrochlorobenzene are also converted to the corresponding chloroaniline with excellent conversion and selectivity under the same reaction conditions (Figure 4b). The slightly lower conversion efficiency of 2-nitrochlorobenzene than 3-nitrochlorobenzene may originate from the steric effect of –Cl in 2-nitrochorobenzene which affects the adsorption of $–NO_2$. Moreover, upon replacement of –Cl with –F, similar results can also be obtained, revealing the excellent catalytic performance of Pt_1/TiO_2-600 for selective conversion of nitroarenes containing various substituent group (Figure 4b).

To understand the origins of the excellent catalytic performance achieved by Pt_1/TiO_2-600, the adsorption behaviors of different functional groups have been investigated by DRIFTS measurements. In the competitive adsorption experiments for the mixture of chlorobenzene (CB) and nitrobenzene (NB) on Pt_1/TiO_2-600, only $–NO_2$ groups (1526 and 1350 cm^{-1}) of NB are adsorbed on Pt_1/TiO_2-600 without CB, indicating the stronger adsorption of

–NO_2 over –Cl (Figure 4c). In contrast, both signals of –NO_2 (1526 and 1350 cm^{-1}) and –Cl groups (742 cm^{-1}) are identified for Pt_{NPs}/TiO_2-400, exhibiting the non-selective absorption (Figure S24). Moreover, the adsorbate-displacement tests have been further conducted and it can be seen that the CB (742 cm^{-1}) pre-adsorbed on Pt_1/TiO_2-600 is readily displaced by post-introduced NB (1526 and 1350 cm^{-1}), further supporting the stronger adsorption of –NO_2 over –Cl on Pt_1/TiO_2-600 (Figure 4d). These results unambiguously explain the superior selectivity of Pt_1/TiO_2-600 in the hydrogenation of *p*-CNB.

In addition, density functional theory (DFT) calculations have been further conducted. The adsorption geometries of *p*-CNB and *p*-CAN on different catalysts are first evaluated (Figure S25–S27). It is found that Pt_1/TiO_2-600 shows similar adsorption energy of *p*-CNB to Pt_{NPs}/TiO_2-400 while possesses much weaker adsorption energy of *p*-CAN, accounting for the better selectivity of Pt_1/TiO_2-600 than Pt_{NPs}/TiO_2-400 (Figure 5a and 5b). Moreover, Pt_1/TiO_2-600 presents much stronger adsorption energy of *p*-CNB (−0.92 eV) than Pt_{1+clus}/TiO_2-800 with the –NO_2 adsorption mode and gives weaker adsorption energy of *p*-CAN (−0.70 eV) (Figure 5a and 5b), well supporting the superior activity of Pt_1/TiO_2-600. Charge distribution calculations shows the negative charge of –NO_2 (0.381 e) is much larger than–Cl (0.007 e), indicating that the –NO_2 group is also more likely attracted on positively charged Pt_1 in Pt_1/TiO_2-600 than the –Cl group (Figure 5c). Moreover, the differential charge density distribution analysis indicates the positively charged Pt_1 is favorable for the adsorption and activation of electron-rich –NO_2 group (Figure 5d). The preferential adsorption of *p*-CNB and easy detachment of *p*-CAN could be responsible for the high activity and selectivity to *p*-CAN over Pt_1/TiO_2-600.

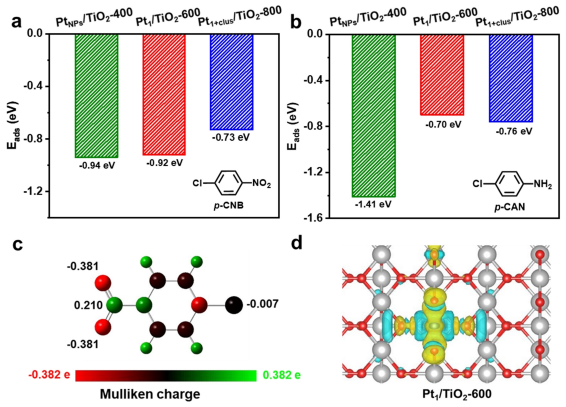

Figure 5. Adsorption energies of (a) *p*-CNB and (b) *p*-CAN on the structures of Pt_{NPs}/TiO_2-400, Pt_1/TiO_2-600 and Pt_{1+clus}/TiO_2-800. (c) Mulliken atomic charge distributions of –NO_2, –Cl in *p*-CNB. (d) The differential charge density distribution of Pt_1/TiO_2-600 at isosurfaces of 0.02 e $Å^{-3}$ (yellow and cyan stands for charge accumulation and depletion). Ti, O, and Pt are shown in silver grey, red, and dark gray spheres, respectively.

Conclusion

In summary, a "sequential thermal transition" strategy has been developed to control the preferential location of single-atom Pt on the outer surface of porous TiO_2 in Pt_1/TiO_2-600 by the pyrolysis of Pt_{NPs}@MIL-125 precursor. When heated at 800 °C under N_2, the Pt_{NPs}@MIL-125 is converted to a composite of Pt_{NPs} and TiO_2 coated by carbon layer (Pt_{NPs}&TiO_2@C-800). Followed by a thermal treatment process at 600 °C in air, the carbon layer of Pt_{NPs}&TiO_2@C-800 is easily burnt off. Meanwhile, the thermal-driven atomization of Pt_{NPs} occurs and the ejected single Pt atoms are captured by pre-formed porous TiO_2. Since the formation of TiO_2 occurs ahead of Pt atomization, the single Pt atoms are preferentially decorated on the outer surface of TiO_2 energetically, generating Pt_1/TiO_2-600 with maximized accessibility (~100 %) of Pt_1 sites. The Pt_1/TiO_2-600 exhibits superior activity and selectivity to all other counterparts, including Pt_{NPs}/TiO_2-400, Pt_{1+clus}/TiO_2-800 and Pt_1@TiO_2-600 with Pt_1 randomly stabilized by TiO_2, in the hydrogenation of *p*-CNB to *p*-CAN. Both experimental and DFT calculation results demonstrate that Pt_1/TiO_2-600 greatly improves the adsorption and activation of –NO_2 group in *p*-CNB while exhibits weak adsorption energy for –Cl of both *p*-CNB and *p*-CAN (targeted product), explaining its excellent performance in the reaction. This work opens a new route to the rational fabrication of single atom catalysts with maximized accessibility of catalytic sites for improved catalysis.

Acknowledgements

This work was supported by the National Key Research and Development Program of China (2021YFA1500400), National Natural Science Foundation of China (22331009, 22222507, 22375193), the Strategic Priority Research Program of the Chinese Academy of Sciences (XDB0450302, XDB0540000), Fundamental Research Funds for the Central Universities (WK2060000038, WK2060000040). We thank 1W1B station at BSRF for the XAFS measurements, the Supercomputing Center of USTC and Hefei Advanced Computing Center. This work was partially carried out at the Instruments Center for Physical Science, University of Science and Technology of China.

Conflict of Interest

The authors declare no conflict of interest.

Data Availability Statement

The data that support the findings of this study are available from the corresponding author upon reasonable request.

Keywords: metal–organic framework · MOF derivatives · single-atom catalysts · selective hydrogenation · accessibility

[1] a) B. Qiao, A. Wang, X. Yang, L. F. Allard, Z. Jiang, Y. Cui, J. Liu, J. Li, T. Zhang, *Nat. Chem.* **2011**, *3*, 634–641; b) C. Wang, S. Mao, Z. Wang, Y. Chen, W. Yuan, Y. Ou, H. Zhang, Y. Gong, Y. Wang, B. Mei, Z. Jiang, Y. Wang, *Chem* **2020**, *6*, 752–765; c) M. Macino, A. J. Barnes, S. M. Althahban, R. Qu, E. K. Gibson, D. J. Morgan, S. J. Freakley, N. Dimitratos, C. J. Kiely, X. Gao, A. M. Beale, D. Bethell, Q. He, M. Sankar, G. J. Hutchings, *Nat. Catal.* **2019**, *2*, 873–881; d) L. L. Li, X. Chang, X. Y. Lin, Z.-J. Zhao, J. L. Gong, *Chem. Soc. Rev.* **2020**, *49*, 8156–8178; e) X. He, H. Zhang, X. Zhang, Y. Zhang, Q. He, H. Chen, Y. Cheng, M. Peng, X. Qin, H. Ji, D. Ma, *Nat. Commun.* **2022**, *13*, 5721; f) R. X. Qin, L. Y. Zhou, P. X. Liu, Y. Gong, K. L. Liu, C. F. Xu, Y. Zhao, L. Gu, G. Fu, N. Zheng, *Nat. Catal.* **2020**, *3*, 703–709; g) R. Lang, X. Du, Y. Huang, X. Jiang, Q. Zhang, Y. Guo, K. Liu, B. Qiao, A. Wang, T. Zhang, *Chem. Rev.* **2020**, *120*, 11986–12043; h) X. Ye, C. Yang, X. Pan, J. Ma, Y. Zhang, Y. Ren, X. Liu, L. Li, Y. Huang, *J. Am. Chem. Soc.* **2020**, *142*, 19001–19005; i) M. J. Hülsey, S. Wang, B. Zhang, S. Ding, N. Yan, *Acc. Chem. Res.* **2023**, *56*, 561–572; j) K. Zhang, Q. Meng, H. Wu, J. Yan, X. Mei, P. An, L. Zheng, J. Zhang, M. He, B. Han, *J. Am. Chem. Soc.* **2022**, *144*, 20834–20846; k) J. R. Ran, A. Talebian-Kiakalaieh, S.-Z. Qiao, *Adv. Energy Mater.* **2024**, *14*, 2400650.

[2] a) H. Zhang, G. Liu, L. Shi, J. Ye, *Adv. Energy Mater.* **2018**, *8*, 1701343; b) T. Zhang, A. G. Walsh, J. Yu, P. Zhang, *Chem. Soc. Rev.* **2021**, *50*, 569–588; c) Y. Li, C.-Q. Xu, C. Chen, Y. Zhang, S. Liu, Z. Zhuang, Y. Zhang, Q. Zhang, Z. Li, Z. Chen, L. Zheng, W.-C. Cheong, K. Wu, G. Jiang, H. Xiao, C. Lian, D. Wang, Q. Peng, J. Li, Y. Li, *J. Am. Chem. Soc.* **2024**, *146*, 20668–20677; d) Y. Pan, Y. Qian, X. Zheng, S.-Q. Chu, Y. Yang, C. Ding, X. Wang, S.-H. Yu, H.-L. Jiang, *Natl. Sci. Rev.* **2021**, *8*, nwaa224; e) L. Ling, X. Guan, X. Liu, X. Lei, Z. Lin, H.-L. Jiang, *Natl. Sci. Rev.* **2024**, *11*, nwae114.

[3] a) Y. Li, S. L. Zhang, W. Cheng, Y. Chen, D. Luan, S. Gao, X. W. Lou, *Adv. Mater.* **2022**, *34*, 2105204; b) Y. Chen, J. Lin, B. Jia, X. Wang, S. Jiang, T. Ma, *Adv. Mater.* **2022**, *34*, 2201796.

[4] a) Y. Wang, J. Mao, X. Meng, L. Yu, D. Deng, X. Bao, *Chem. Rev.* **2019**, *119*, 1806–1854; b) X. Xie, L. Peng, H. Yang, G. I. N. Waterhouse, L. Shang, T. Zhang, *Adv. Mater.* **2021**, *33*, 2101038; c) Y. Wang, D. Wang, Y. Li, *Adv. Mater.* **2021**, *33*, 2008151; d) L. Liu, A. Corma, *Chem. Rev.* **2023**, *123*, 4855–4933.

[5] a) H. Furukawa, K. E. Cordova, M. O'Keeffe, O. M. Yaghi, *Science* **2013**, *341*, 1230444; b) H. C. J. Zhou, S. Kitagawa, *Chem. Soc. Rev.* **2014**, *43*, 5415–5418; c) T. Islamoglu, S. Goswami, Z. Li, A. J. Howarth, O. K. Farha, J. T. Hupp, *Acc. Chem. Res.* **2017**, *50*, 805–813; d) X. Zhao, Y. Wang, D.-S. Li, X. Bu, P. Feng, *Adv. Mater.* **2018**, *30*, 1705189; e) R.-B. Lin, S. Xiang, W. Zhou, B. Chen, *Chem* **2020**, *6*, 337–363; f) L. Jiao, Y. Wang, H.-L. Jiang, Q. Xu, *Adv. Mater.* **2018**, *30*, 1703663; g) L. Jiao, J. Wang, H.-L. Jiang, *Acc. Mater. Res.* **2021**, *2*, 327–339; h) L. Jiao, H.-L. Jiang, *Chin. J. Catal.* **2023**, *45*, 1–5; i) G. Li, S. Zhao, Y. Zhang, Z. Tang, *Adv. Mater.* **2018**, *30*, 1800702.

[6] a) L. Jiao, H.-L. Jiang, *Chem* **2019**, *5*, 786–804; b) C. Wang, Y. Yao, J. Li, Y. Yamauchi, *Acc. Mater. Res.* **2022**, *3*, 426–438; c) H. Huang, K. Shen, F. Chen, Y. Li, *ACS Catal.* **2020**, *10*, 6579–6586; d) Y.-Z. Chen, R. Zhang, L. Jiao, H.-L. Jiang, *Coord. Chem. Rev.* **2018**, *362*, 1–23; e) X. Han, T. Zhang, X. Wang, Z. Zhang, Y. Li, Y. Qin, B. Wang, A. Han, J. Liu, *Nat. Commun.* **2022**, *13*, 2900; f) S. Liu, C. Li, M. J. Zachman, Y. Zeng, H. Yu, B. Li, M. Wang, J. Braaten, J. Liu, H. M. Meyer, M. Lucero, A. J. Kropf, E. E. Alp, Q. Gong, Q. Shi, Z. Feng, H. Xu, G. Wang, D. J. Myers, J. Xie, D. A. Cullen, S. Litster, G. Wu, *Nat. Energy* **2022**, *7*, 652–663; g) S. Wei, A. Li, J.-C. Liu, Z. Li, W. Chen, Y. Gong, Q. Zhang, W.-C. Cheong, Y. Wang, L. Zheng, H. Xiao, C. Chen, D. Wang, Q. Peng, L. Gu, X. Han, J. Li, Y. Li, *Nat. Nanotechnol.* **2018**, *13*, 856–861; h) T. De Villenoisy, X. Zheng, V. Wong, S. Mofarah, H. Arandiyan, Y. Yamauchi, P. Koshy, C. Sorrell, *Adv. Mater.* **2023**, *35*, 2210166; i) H. Zhang, H.-C. Chen, S. Feizpoor, L. Li, X. Zhang, X. Xu, Z. Zhuang, Z. Li, W. Hu, R. Snyders, D. Wang, C. Wang, *Adv. Mater.* **2024**, *36*, 2400523; j) L. Wang, J. Wan, Y. Zhao, N. Yang, D. Wang, *J. Am. Chem. Soc.* **2019**, *141*, 2238–2241.

[7] a) G. Chen, Y. An, S. Liu, F. Sun, H. Qi, H. Wu, Y. He, P. Liu, R. Shi, J. Zhang, A. Kuc, U. Kaiser, T. Zhang, T. Heine, G. Wu, X. Feng, *Energy Environ. Sci.* **2022**, *15*, 2619–2628; b) I. Song, Y. Eom, M. Austeria, D. H. Hong, M. Balamurugan, R. Boppella, D. H. Kim, T. K. Kim, *Small* **2023**, *19*, 2300049.

[8] a) H. Li, Q. Wan, C. Du, Q. Liu, J. Qi, X. Ding, S. Wang, S. Wan, J. Lin, C. Tian, L. Li, T. Peng, W. Zhao, K. H. L. Zhang, J. Huang, X. Zhang, Q. Gu, B. Yang, H. Guo, S. Lin, A. K. Datye, Y. Wang, H. Xiong, *Chem* **2022**, *8*, 731–748; b) J. Xu, C. Zhang, H. Liu, J. Sun, R. Xie, Y. Qiu, F. Lü, Y. Liu, L. Zhuo, X. Liu, *Nano Energy* **2020**, *70*, 104529.

[9] J.-D. Xiao, L. Han, J. Luo, S.-H. Yu, H.-L. Jiang, *Angew. Chem. Int. Ed.* **2018**, *57*, 1103–1107.

[10] a) W. Wan, J. Geiger, N. Berdunov, M. L. Luna, S. W. Chee, N. Daelman, N. Lopez, S. Shaikhutdinov, B. R. Cuenya, *Angew. Chem. Int. Ed.* **2022**, *61*, e202112640; b) A. Bruix, Y. Lykhach, I. Matolinova, A. Neitzel, T. Skala, N. Tsud, M. Vorokhta, V. Stetsovych, K. Sevcikova, J. Myslivecek, R. Fiala, M. Vaclavu, K. C. Prince, S. Bruyere, V. Potin, F. Illas, V. Matolin, J. Libuda, K. M. Neyman, *Angew. Chem. Int. Ed.* **2014**, *53*, 10525–10530.

[11] X. Cheng, Y. Li, L. Zheng, Y. Yan, Y. Zhang, G. Chen, S. Sun, J. Zhang, *Energy Environ. Sci.* **2017**, *10*, 2450–2458.

[12] a) F. Maurer, J. Jelic, J. Wang, A. Gänzler, P. Dolcet, C. Wöll, Y. Wang, F. Studt, M. Casapu, J. D. Grunwaldt, *Nat. Catal.* **2020**, *3*, 824–83; b) S. Xie, L. Liu, Y. Lu, C. Wang, S. Cao, W. Diao, J. Deng, W. Tan, L. Ma, S. N. Ehrlich, Y. Li, Y. Zhang, K. Ye, H. Xin, M. Flytzani-Stephanopoulos, F. Liu, *J. Am. Chem. Soc.* **2022**, *144*, 21255–21266.

[13] a) H. Jeong, D. Shin, B. S. Kim, J. Bae, S. Shin, C. Choe, J. W. Han, H. Lee, *Angew. Chem. Int. Ed.* **2020**, *132*, 20872–20877; b) Y. Si, Y. Jiao, M. Wang, S. Xiang, J. Diao, X. Chen, J. Chen, Y. Wang, D. Xiao, X. Wen, N. Wang, D. Ma, H. Liu, *Nat. Commun.* **2024**, *15*, 4887.

[14] a) J. Jones, H. Xiong, A. T. Delariva, E. J. Peterson, H. Pham, S. R. Challa, G. Qi, S. Oh, M. H. Wiebenga, X. I. P. Hernandez, Y. Wang, A. K. Datye, *Science* **2016**, *353*, 150–154; b) H. Xiong, D. Kunwar, D. Jiang, C. Garcia-Vargas, H. Li, C. Du, G. Canning, X. Pereira-Hernandez, Q. Wan, S. Lin, S. Purdy, J. Miller, K. Leung, S. Chou, H. Brongersma, R. Ter Veen, J. Huang, H. Guo, Y. Wang, A. K. Datye, *Nat. Catal.* **2021**, *4*, 830–839; c) M. Moliner, J. E. Gabay, C. E. Kliewer, R. T. Carr, J. Guzman, G. L. Casty, P. Serna, A. Corma, *J. Am. Chem. Soc.* **2016**, *138*, 15743–15750.

[15] a) J. Zhang, L. Wang, Y. Shao, Y. Wang, B. C. Gates, F.-S. Xiao, *Angew. Chem. Int. Ed.* **2017**, *56*, 9747–9751; b) R. V. Jagadeesh, A.-E. Surkus, H. Junge, M.-M. Pohl, J. Radnik, J. Rabeah, H. Huan, V. Schünemann, A. Brückner, M. Beller, *Science* **2013**, *342*, 1073–1076.

Manuscript received: October 1, 2024
Accepted manuscript online: October 29, 2024
Version of record online: November 16, 2024